Supplementary Information

Charge and spin delocalisation in photoinduced polarons of polymer donors and non-fullerene acceptors for organic photovoltaics - A multi-frequency pulse EPR study

Jack M.S. Palmer,[a] Oliver Christie,[a], Claudia E. Tait*[a]

[a] *Department of Chemistry, University of Oxford, Oxford OX1 3QZ, United Kingdom.*

Contents

Experimental methods

S1 Sample preparation

The donor polymers PBDB-T and PM6 and acceptor molecules ITIC and Y6 were purchased from 1-Material and the $PC_{61}BM$ acceptor was purchased from Ossila. The sample preparation was performed in a glovebox under nitrogen atmosphere. Solutions were prepared in chlorobenzene (anhydrous, purity 99.8%, Sigma-Aldrich) for the PBDB-T blends and in chloroform (anhydrous, purity $\geq 99\%$, Sigma-Aldrich) for the PM6 blends. Initially, $20\,mg\,mL^{-1}$ stock solutions were prepared for each material and stirred at 40 °C and 500 rpm for about three hours. Blend solutions were then prepared by mixing donor and acceptor solutions in a ratio of 1:1.5 for PBDB-T:$PC_{61}BM$,[1,2] 1:1 for PBDB-T:ITIC,[3] 1:1.2 for PM6:$PC_{61}BM$,[4] and 1:1.2 for PM6:Y6,[5] and stirred over night at room temperature.

For the X- and Q-band EPR measurements, samples were prepared by transferring 30 μL of the blend solutions, diluted to $10\,mg\,mL^{-1}$, into 2.0 mm ID, 2.9 mm OD quartz EPR tubes, evaporating the solvent under vacuum to create a film on the inside of the EPR tube and flame-sealing the tube after backfilling with helium.

For the W-band EPR measurements, powder samples were prepared from drop-cast films by scratching fragments of the films off a glass substrate with a scalpel and transferring them into 0.70 mm ID, 0.87 mm OD quartz EPR tubes up to a fill height of about 2 mm. The quality of the powder samples was verified by checking for invariance of the recorded EPR spectrum for two different sample orientations differing by 90°.

S2 EPR measurements

X-band pulse EPR measurements were performed on a Bruker ElexSys E680 spectrometer with a Bruker EN 4118X-MD4 resonator and 1 kW Applied Systems Engineering TWT amplifier. Q-band pulse EPR measurements were performed on a Bruker ElexSys E580 spectrometer with a a TE011 cylindrical cavity Q-band resonator with large sample access and optical window,[6] built by the mechanical engineering workshop of the

Physics department at the FU Berlin, and a 150 W TWT amplifier. W-band pulse EPR measurements were performed on a Bruker ElexSys E680 spectrometer with a Bruker Teraflex EN600-1021H resonator. All spectrometers were equipped with Oxford Instruments helium-flow cryostats and temperature control systems and all experiments were performed at a temperature of 20 K. A field calibration using an N@C_{60} g-standard[7] was performed before the EPR measurements at all frequency bands.

At X- and Q-band, the samples were illuminated through the optical window of the cryostat with depolarised light from an EKSPLA NT230 tuneable diode-pumped laser system set to 532 nm and 0.25 to 1 mJ at 50 Hz. To achieve steady-state measurements, the laser and spectrometer were not synchronised. Some of the Q-band measurements were also performed using constant white-light illumination with a Schott DCR III 150 W halogen light source, giving equivalent spectra to non-synchronised laser excitation. At W-band, the samples were illuminated using a continuous-wave 532 nm diode-pumped solid state laser (Thorlabs DJ532-10) with an optical output power of 10 mW. The light was focused into an optical fibre fed through the sample holder and inserted into the W-band EPR tube with the tip of the fibre at a distance of about 1 cm from the bottom of the tube. Reference measurements without illumination were performed immediately after inserting the samples into the cryostat (with covered optical window at X- and Q-band) before illumination.

S2.1 Echo-detected field sweeps

At X-band, pulse EPR spectra were recorded as echo-detected field sweeps with a two-pulse echo sequence with pulse lengths of $t_{\pi/2}$ =50 ns and t_π =100 ns, an inter-pulse delay τ =300 ns. At Q-band, pulse lengths of $t_{\pi/2}$ =60 ns and t_π =120 ns and an inter-pulse delay τ =400 ns were used. At W-band, the pulse lengths were $t_{\pi/2}$ =60 ns and t_π =120 ns and the inter-pulse delay was τ =400 ns. A two-step phase cycle on the first pulse was used in all cases.

S2.2 Relaxation time measurements

Echo decay measurements were performed using the pulse sequence $\frac{\pi}{2}-\tau-\pi-\tau-$echo with $t_{\pi/2}$ =60 ns, t_π =120 ns, τ_0 =500 ns and a two-step phase cycle.

Inversion recovery measurements were performed with the pulse sequence $\pi_{\text{inv}}-T-\frac{\pi}{2}-\tau-\pi-\tau-$echo, with an initial inversion pulse of $t_{\pi,\text{inv}}$ =60 ns and an echo detection sequence with $t_{\pi/2}$ =60 ns, t_π =120 ns, τ =400 ns with a four-step phase cycle. At W-band, the inversion recovery experiments were performed as a function of magnetic field.

S2.3 ELDOR-detected NMR measurements

ELDOR-detected NMR experiments were performed at W-band with the pulse sequence HTA$-T-\frac{\pi}{2}-\tau-\pi-\tau-$echo, with a high-turning angle (HTA) pulse of 40 μs (on the spectrometer's ELDOR channel), T =4 μs and an echo detection sequence with $t_{\pi/2}$ =120 ns, t_π =240 ns, τ =500 ns with a two-step phase cycle. The length and intensity of the HTA pulse were tuned to minimise the central Lorentzian hole and maximise the intensity of the peaks centred at the ^{14}N Larmor frequency. The frequency of the HTA pulse was swept over 50 MHz around the frequency of the detection sequence. ELDOR-detected NMR experiments were performed both as a function of magnetic field and additionally at selected magnetic field positions. EDNMR-induced EPR experiments were performed by setting the HTA pulse frequency on-resonance ($\nu_{\text{obs}} = +10$ MHz) and off-resonance ($\nu_{\text{obs}} = +30$ MHz) and sweeping the magnetic field.

S2.4 Davies ENDOR measurements

W-band Davies ENDOR measurements were performed with the pulse sequence $\pi-T-\frac{\pi}{2}-\tau-\pi-\tau-$echo with t_π =120 ns, $t_{\pi/2}$ =60 ns, t_π =120 ns, τ =280 ns and a 40 μs radiofrequency π pulse applied during the delay T, with delays of 2 μs between the radiofrequency and microwave pulses.

For Q-band Davies ENDOR measurements, t_π =120 ns, $t_{\pi/2}$ =60 ns, t_π =120 ns, τ =350 ns and $t_{\pi,\text{rf}}$ =28 μs, with delays of 2 μs between the radiofrequency and microwave pulses.

W-band Mims ENDOR measurements were performed with the pulse sequence $\frac{\pi}{2}-T-\frac{\pi}{2}-\tau-\pi-\tau-$echo with $t_{\pi/2}$ =30 ns, τ =160 ns and a 40 μs radiofrequency π pulse applied during the delay T.

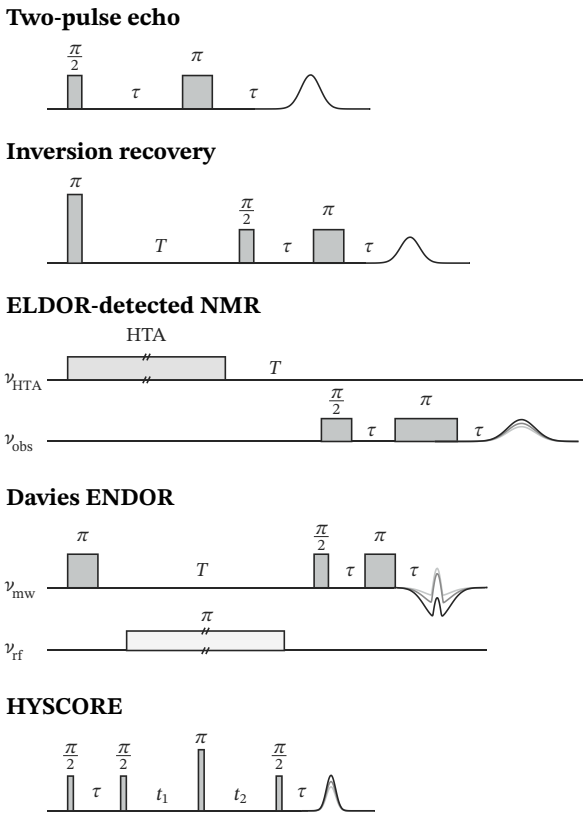

Fig. S1 Pulse sequences for the two-pulse echo, inversion recovery, ELDOR-detected NMR, Davies ENDOR and HYSCORE experiments used in this work.

For the W-band ENDOR experiments, an Amplifier Research 150 W RF amplifier was used, while a Bruker 150 W RF amplifier was used for the Q-band ENDOR measurements. The radiofrequency pulse length was adjusted for ^{1}H using a Rabi nutation experiment. The frequency of the radiofrequency pulse was varied stochastically.

S2.5 HYSCORE measurements

HYSCORE experiments were performed at Q-band with the pulse sequence $\frac{\pi}{2}-\tau-\frac{\pi}{2}-t_1-\pi-t_2-\frac{\pi}{2}-\tau-$echo with $t_{\pi/2}$ =20 ns, t_π =20 ns, τ =164, 224 and 304 ns, starting t_1 and t_2 values of 96 ns and time increments of 16 ns and 200 points in both the t_1 and t_2 dimension. An 8-step phase cycle[8] was used to remove contributions from unwanted coherence transfer pathways.

The experimental time-domain data was baseline-corrected with a 5$^{\text{th}}$ order-polynomial, apodised in both dimensions with a Hamming window, zero-filled to four times the initial number of data points and Fourier transformed in both dimensions. The resulting HYSCORE spectrum was symmetrised and the results obtained for the three different τ values were combined.

S3 Density Functional Theory calculations

All DFT calculations were performed with the ORCA program system[9–14] (version 5.0.4).

For the polymer donors PBDB-T and PM6, models consisting of increasing numbers of repeat units (n = 1, 2, 2.5D, 2.5A, 3, 3.5D, 3.5A, 4, where D and A denote the donor or acceptor part of the repeat unit) were constructed. The sidechains were truncated to methyl groups to reduce computational costs. For the non-fullerene acceptors, in addition to models of the single molecules with truncated side chains, calculations were also performed for single molecules extracted from different reported crystal structures,[5,15–17] in part containing the full side chains. In addition to individual molecules, pairs of $\pi-\pi$-stacked non-fullerene acceptor molecules were also modelled based on the ITIC[15] and Y6[17] crystal structures. The different pairs of molecules identified and extracted from the single crystal X-ray data are shown in Fig. S11.

Geometry optimisations were performed first for the ground state and then for the radical cation state for the donors and the radical anion state for the acceptors using either the GGA functional BP86 or the range-separated hybrid functional ωB97X-D4[18,19] and the def2-SVP basis set, including a dispersion correction.[20–26] Calculations were performed for both the default range-separation parameter ω (= 0.25 a_0^{-1}) as well as an ω value individually tuned for each of the investigated molecules following procedures described in the literature.[27–29] The optimal range-separation parameter was selected by matching the HOMO eigenvalue with the ionisation potential for donor radical cations or the LUMO eigenvalue with the electron affinity for acceptor radical anions. The optimised values of $\omega_{\text{opt}} = 0.11-0.12\,a_0^{-1}$ are in agreement with ranges previously determined for other organic semiconducting donor polymers.[30,31] In all calculations, a conductor-like polarisable continuum model (CPCM) with a dielectric constant of ϵ =3.5 was chosen to model effects of the environment in an organic semiconductor film.[32–34]

Magnetic parameters (g-values, hyperfine and nuclear quadrupole couplings)[35–38] were calculated for the optimised radical cation or radical anion geometries using either the hybrid PBE0 functional or the range-separated hybrid ωB97X-D4[18,19] functional and the EPR-II basis set for H, C, N, O and F and the IGLO-II basis set for S.[39–42]

S4 Data analysis and simulations

Simulations of the echo-detected EPR spectra, the ENDOR spectra and the HYSCORE spectra were performed with the EasySpin simulation toolbox[43,44] (version 6.0) in Matlab.

S4.1 Global fit of multi-frequency EPR data

The g-values, g-strains and linewidths characterising the EPR spectra of the positive polarons on the donor polymers, PBDB-T$^{\bullet+}$ and PM6$^{\bullet+}$, and the negative polarons on the acceptor molecules, PC$_{61}$BM$^{\bullet-}$, ITIC$^{\bullet-}$ and Y6$^{\bullet-}$, were determined through global fitting of the EPR spectra recorded at X-, Q- and W-band frequencies shown in Fig. 2 in the main text, as well as the W-band EPR spectra extracted for the non-fullerene acceptors ITIC and Y6 by EDNMR-induced EPR spectroscopy (Fig. 3) and relaxation-filtered inversion recovery experiments (Fig. S3). The global fitting procedure used the fitting algorithms implemented in EasySpin[43] with weights empirically adjusted to reflect the information content of the individual spectra.

A fixed set of g-values and selected g-strains were used to fit all spectra of a single blend recorded at different frequencies, and were additionally constrained to the same values for PBDB-T$^{\bullet+}$, PM6$^{\bullet+}$ and PC$_{61}$BM$^{\bullet-}$ in each of the blends containing these donor and acceptor molecules. Convolutional Gaussian linewidths were used to model broadening due to unresolved hyperfine couplings and were individually adjusted for each experimental spectrum. The resulting set of best-fit parameters are listed in Table 1 in the main text.

Simulation of the X-band EPR spectra of ITIC$^{\bullet-}$ and Y6$^{\bullet-}$ required the additional inclusion of hyperfine couplings, which were extracted from DFT calculations performed on single molecules of ITIC and Y6. For ITIC, simulations were performed including two pairs of two coupled protons, the protons on the vinyl linkers (A = [−5.4, −12.0, −16.4] MHz, Euler angles of 321°, 90° and 89° with respect to the g-frame) and the protons on the edges of the central indacenodithienothiophene (IDTT) (A = [−3.7, −7.6, −9.7] MHz, Euler angles of 316°, 90° and 89° with respect to the g-frame). For Y6, the pair of protons on the vinyl linkers (A = [−5.0, −10.9, −15.0] MHz, Euler angles of 225°, 91° and 85° and 312°, 79° and 87° with respect to the g-frame) and

a pair of fluorine nuclei on terminal 1,1-dicyanomethylene-3-indanone (INCN) groups ($A=[-1.1,-2.8,-16.4]$ MHz, Euler angles of 309°, 6° and 239° and 130°, 11° and 220° with respect to the g-frame) were included in the simulations.

S4.2 ENDOR simulations based on DFT results

ENDOR simulations were performed in EasySpin[43] using the experimentally determined g-values and hyperfine interaction parameters (principal values and relative orientations of the g- and A-frames) predicted by DFT calculations performed using the ORCA software package. Simulations were performed for each coupled nucleus individually and then summed. An ENDOR linewidth of 1 MHz was used to account for some degree of distribution of hyperfine parameters. Orientation-selection effects were included in the simulations by assuming a 20 MHz excitation bandwidth.

S4.3 Regularised least-squares fitting of ENDOR data

The regularised least-squares fitting of the ENDOR data guided by predictions from DFT calculations was based on the procedure described by Pribitzer, Mannikko and Stoll,[45] using scripts adapted from the ones provided with their publication.

Least-squares fitting of the set of W-band ENDOR spectra recorded as a function of magnetic field was performed using Tikhonov-type regularisation. The best-fit probability distribution over the hyperfine parameter space, P_{fit} is determined by solving the following minimisation problem:

$$P_{\mathrm{fit}} = \arg\min_{P\geq 0}\left(\left|\left|S_{\mathrm{exp}} - KP\right|\right|^2 + \lambda^2 \left|\left|\Gamma_P P\right|\right|^2\right)$$

where S_{exp} is the experimental ENDOR data, $P(a_{\mathrm{iso}},T,\eta,\alpha,\beta,\gamma)$ is the probability distribution over the hyperfine parameter space, K is a kernel matrix containing the simulated ENDOR data for each set of parameters $\left(a_{\mathrm{iso},i},T_i,\eta_i,\alpha_i,\beta_i,\gamma_i\right)$ along the columns, λ is the regularisation parameter and Γ_P is the regularisation operator. The first term is the usual residual norm of standard least-squares fitting, which minimises the discrepancy between the experimental data and the simulation for a certain weighted distribution of hyperfine parameters defined by the probability distribution P, whereas the second one is a penalty term that favours probability distributions that do not deviate too strongly from a prior probability distribution, estimated based on the DFT predictions. As proposed by Pribitzer et al.,[45] the regularisation operator Γ_P was defined as

$$\Gamma_P = -\ln P_{\mathrm{DFT}}$$

similar to the cross entropy between P_{DFT} and P.

The probability distribution, and therefore the kernel matrix, span the full hyperfine parameter space required to model the experimental data. In the present cases, a wide range of hyperfine interactions contributes to the ENDOR spectra, therefore in order to model this in a completely general way, the hyperfine interaction of each single nucleus is described in terms of an isotropic hyperfine interaction constant a_{iso}, a dipolar hyperfine coupling parameter T and a rhombicity parameter η ($0\leq\eta\leq 1$), defining the extent of deviation from axial symmetry. The resulting hyperfine matrix in the principal axis frame is constructed as follows:

$$\boldsymbol{A} = \begin{pmatrix} a_{\mathrm{iso}} - T(1-\eta) & 0 & 0 \\ 0 & a_{\mathrm{iso}} - T(1+\eta) & 0 \\ 0 & 0 & a_{\mathrm{iso}} + 2\,T \end{pmatrix}$$

Additionally, three Euler angles, α, β and γ, defining the orientation of the principal axis system with respect to the g-frame, are required to reproduce orientation selection effects in the ENDOR spectra recorded as a function of magnetic field. The probability distribution and kernel matrix therefore need to span a six-dimensional parameter space with sufficient resolution. The setup of the parameter grid for the fitting was adapted to avoid the matrices becoming prohibitively large for this higher-dimensional fitting problem. The parameter space was reduced significantly by replacing the full three-dimensional Euler angle space with a one-dimensional set of combinations of three Euler angles based on the results of DFT calculations for a series of molecular models. This is based on the high accuracy of DFT predictions of the orientation of hyperfine principal axis systems for aromatic organic systems, in agreement with simple considerations that have been experimentally validated.[46] The validity of this assumption is further confirmed by the agreement between the experimentally observed orientation selection effects and the trends in ENDOR spectra simulated based on DFT predictions (section 2.2.2). The Euler angles for all protons in the DFT models were projected onto a coarse grid with a 5 or 15° resolution to give a unique set of angle combinations. In order to cover the remaining parameter space with a grid of sufficient resolution, a set of five calculations over offset coarse grids for a_{iso}, T and η were performed and combined, resulting in a finer grid with a resolution of 0.2 MHz, 0.04 MHz and 0.04 for a_{iso}, T and η, respectively, in the case of the polymer donors PBDB-T$^{\bullet+}$ and PM6$^{\bullet+}$, and 0.4 MHz, 0.1 MHz and 0.04 for the non-fullerene acceptors ITIC$^{\bullet-}$ and Y6$^{\bullet-}$. Typical sizes for the individual grids were in the range of 25 000 to 100 000 points.

The kernel matrix was computed for the defined hyperfine parameter space using EasySpin,[43] with an intrinsic ENDOR linewidth of 0.1 MHz and by modelling orientation selection with an excitation bandwidth of 16 MHz. The simulations were performed with the spin system parameters determined from the analysis of the EPR spectra at multiple frequencies in section 2.1 and summarised in Table 1. The simulated ENDOR spectra were multiplied by the Davies ENDOR intensity envelope function to account for the hyperfine selectivity determined by the initial inversion pulse[47]

$$V_{\mathrm{Davies}} \propto \frac{\sqrt{2}\left|2(\nu_{\mathrm{rf}} - \nu_{1\mathrm{H}})\right| t_{\mathrm{p}}}{2(\nu_{\mathrm{rf}} - \nu_{1\mathrm{H}})^2 t_{\mathrm{p}}^2 + \frac{1}{2}}$$

For each grid point, ENDOR spectra simulated at different field positions were concatenated, preserving their relative in-

tensities.

Prior probability distributions P_{DFT} were constructed by defining multi-variate Gaussian functions over the hyperfine parameter space with widths of $\sigma_{a_{\mathrm{iso}}}$ =0.2 MHz, σ_T =0.2 MHz, σ_η =0.05 and $\sigma_{\alpha/\beta/\gamma}$ =0.2 rad. This is based on a simple extension of the approach described by Pribitzer et al.[45] to the higher-dimensional parameter space. The priors included DFT predictions for models with $n = 1$-4 repeat units for the donor polymers PBDB-T$^{\bullet+}$ and PM6$^{\bullet+}$. For the non-fullerene acceptors, calculations were performed with priors just including DFT predictions for single ITIC and Y6 molecules or additionally including DFT predictions for pairs of molecules modelled based on the reported crystal structures. The priors and the DFT predictions they are based on are summarised in Fig. S19.

The regularised least-squares fitting with the penalty term defined based on the DFT-derived prior P_{DFT} was performed exactly as described by Pribitzer et al.[45] using a fast non-negative least-squares algorithm.[48] In order to account for incomplete suppression at the Larmor frequency due to the change in local field caused by the simultaneous inversion of a large number of very weakly coupled spins,[49] a matrix peak modelled as a Lorentzian was added to the kernel, separately for ENDOR spectra acquired at different magnetic fields. In the case of the ENDOR spectra of the PBDB-T:ITIC and PM6:Y6 blends containing contributions from both the donor and acceptor polarons, the donor contribution determined from the experimental spectra recorded for PBDB-T:$PC_{61}BM$ and PM6:$PC_{61}BM$ were included in the kernel and added with a fixed amplitude determined by the relative contribution of the two species at each field position.

The regularisation parameter λ was selected based on a combination of the L-curve criterion and visual inspection of the results, as more advanced approaches for the selection of the optimal regularisation parameter, such as the Akaike information criterion,[45] resulted in high memory and computation time requirements. Values of $\lambda = 200$ were used for PBDB-T$^{\bullet+}$ and PM6$^{\bullet+}$, while values of $\lambda = 6$ and $\lambda = 10$ were used for ITIC$^{\bullet-}$ and Y6$^{\bullet-}$, respectively. Only minor changes in the resulting probability distributions were observed for λ values in a small range around the selected values, whereas lower regularisation parameters led to broader probability distributions and higher parameters to a worse agreement with the experimental results. In all cases, the fitting was performed for a range of different priors including individual DFT models, subsets or the complete set of models, giving consistent results and validating the adapted approach for the purposes of the mostly qualitative analysis of the fitting results in this work. The probability distributions shown here were obtained as the average of results from a series of different fits.

Inspection of individual contributions to the ENDOR spectra simulated based on the hyperfine parameter probability distributions determined with this regularised least-squares fitting procedure and comparison to the DFT-predicted hyperfine interaction parameters confirms that the most probable contributions are in good agreement with the DFT-predicted hyperfine coupling strength, anisotropy and principal axis orientations and reflect a distribution around these values, accounting for the heterogeneity of molecular environments in the investigated systems and for uncertainties in DFT calculations.

S4.4 HYSCORE simulations based on DFT results

HYSCORE simulations were performed in EasySpin[43,44] using the experimentally determined g-values and nuclear quadrupole and hyperfine interaction parameters hyperfine interaction parameters (principal values and relative orientations of the g-, A-frames and Q-frames) predicted by DFT calculations. Simulations were performed for a spin system including all coupled nitrogen nuclei. The simulated time-domain traces were converted into the frequency domain data shown in the figures using the same analysis routine as for the experimental data (section S2.5). Orientation-selection effects were included in the simulations by assuming a 50 MHz excitation bandwidth and, in analogy to experiment, simulations were performed for three different τ values and summed.

Additional experimental data

S5 Dark and light EPR spectra

For all samples, reference echo-detected EPR spectra were recorded in the dark immediately after sample insertion and are compared to the spectra obtained during illumination in Fig. S2. The "dark" spectra contain contributions from any background signals of the resonator as well as intrinsic paramagnetic defects. The optical window of the resonator was covered for the acquisition of these dark reference signals, as even stray ambient light was found to generate a small amount of light-induced polarons. The results in Fig. S2 clearly show only very minor contributions prior to illumination, which in most cases are limited to the field range corresponding to the donor polymer signal, suggesting the presence of a small contribution of paramagnetic states on the polymer chains.

When the light was turned off, about 30-40% of the light-induced signals decayed over a time-span of about 30 minutes, suggesting recombination of mobile charged states, while the remaining signals persisted and are attributed to charges trapped at 20 K. At higher temperatures, an increasing fraction of light-induced states decayed by recombination after illumination, and at room temperature the steady-state concentration of charged states was below the detection limit of EPR.

S6 Disentangling spectral contributions by relaxation-filtered EPR

The overlapping signatures of polarons on donor and acceptor molecules for the non-fullerene acceptor blends can also be separated by exploiting differences in relaxation times.[34,50,51] In principle, the two spectral contributions for species characterised by different relaxation times can be extracted by performing an inversion recovery experiment using a filter time T_F corresponding to the zero-crossing point of the inversion recovery trace of each of the individual components. The extensive spectral overlap of the donor and acceptor polaron components in this case, in particular the possibility that the acceptor contribution extends across the full width of the donor spectrum, prevents the isolation of inversion recovery traces that can clearly be attributed to a single species. Therefore, a two-dimensional inversion recovery experiment was performed with the magnetic field as the second dimension, and the filter times were selected by considering slices extracted for different inversion recovery delays. The accurate extraction of overlapping spectral signatures using the relaxation-filtered EPR approach relies on the absence of significant T_1 anisotropy, which was verified for the donor polymers based on field-dependent inversion recovery experiments performed for the PBDB-T:$PC_{61}BM$ and PM6:$PC_{61}BM$ blends.

The results of W-band inversion recovery experiments performed as a function of magnetic field for PBDB-T:ITIC and PM6:Y6 are displayed in Fig. S3. The experimental results

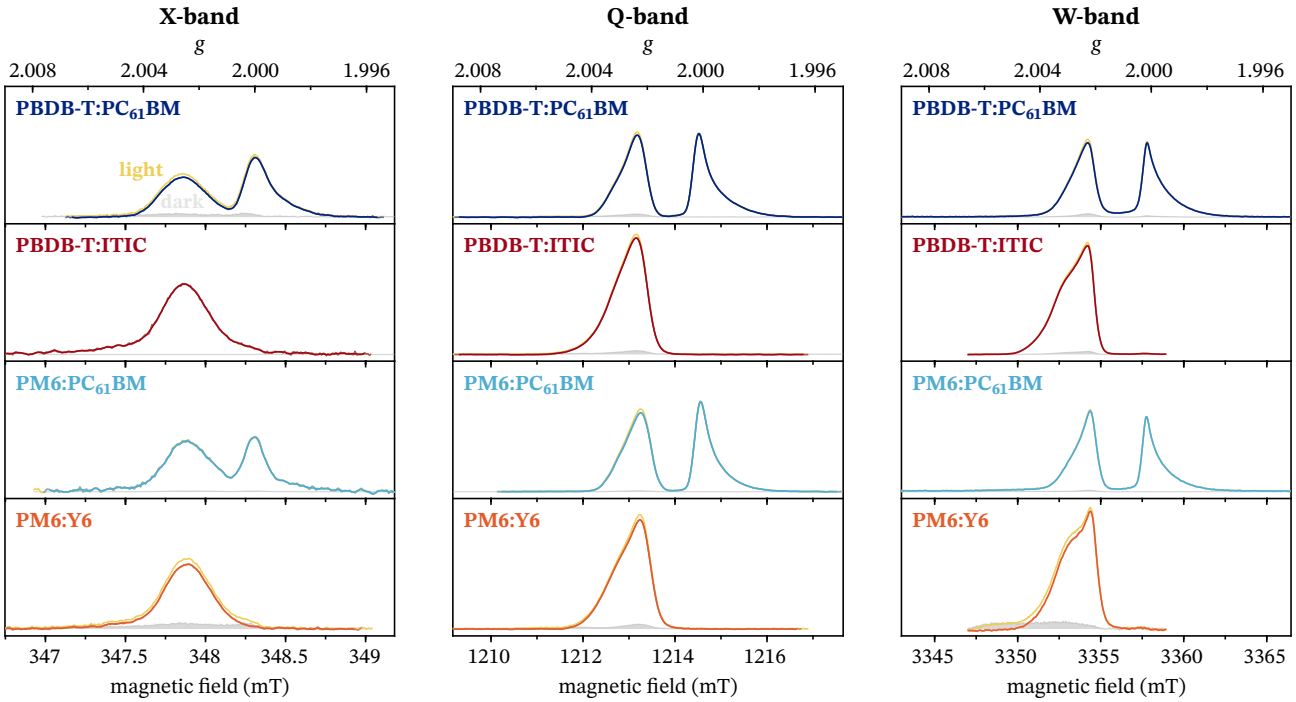

Fig. S2 X-, Q- and W-band echo-detected EPR spectra recorded at 20 K for the PBDB-T:$PC_{61}BM$, PBDB-T:ITIC, PM6:$PC_{61}BM$ and PM6:Y6 blends in the dark (grey, recorded immediately after sample insertion) and under constant illumination (yellow), as well as the light-induced spectra obtained after subtraction of the dark background signals. Further experimental details are described in section S2.1.

show a gradual shift in the position of the zero-crossing point of the inversion recovery trace towards earlier times at higher magnetic fields. Inversion recovery traces extracted at the low-field end of the spectrum, where the polaron on the acceptor is expected to almost exclusively contribute to the spectrum based on the donor polaron signature determined for the corresponding fullerene acceptor-based blends, and at the maximum of the donor polaron spectrum, towards the high-field end of the spectrum, are compared in the right panels. For both non-fullerene acceptor-based blends, a longer T_1 relaxation time is observed at lower magnetic fields and assigned to the polaron localised on the acceptor. In order to extract the corresponding spectral contribution, we inspected slices extracted at inversion delays close to the zero-crossing point of the inversion recovery trace extracted at the high-field position and selected the spectrum without discontinuities around the field position corresponding to the maximum, where PBDB-T$^{\bullet+}$ or PM6$^{\bullet+}$ contribute most significantly to the overall spectrum. This resulted in the filter time T_F =1.3 ms for PBDB-T:ITIC and T_F =1.9 ms for PM6:Y6 and the spectra shown in the top panels of Fig. S3. Similarly, the spectral contributions of the donor polarons were extracted from slices close to the zero-crossing point of inversion recovery traces recorded at the low-field edge of the spectrum, resulting in filter times T_F =15.3 ms for PBDB-T:ITIC and T_F =11.0 ms for PM6:Y6. The corresponding spectra are in good agreement with simulations based on the parameters extracted for PBDB-T$^{\bullet+}$ and PM6$^{\bullet+}$ by fitting of the PBDB-T:$PC_{61}BM$ and PM6:$PC_{61}BM$ EPR spectra. The sum of the two contributions was verified to match the overall spectrum obtained with a simple two-pulse echo sequence without inversion pulse.

The ITIC$^{\bullet-}$ and Y6$^{\bullet-}$ contributions extracted using this relaxation-filter approach are in good agreement with the spectra obtained by EDNMR-induced EPR (Fig. 3 in the main text), validating the selection of filter times and suggesting this approach may be used to disentangle overlapping spectral contributions that cannot be separated by exploiting coupling to magnetic nuclei unique to one of the components.

Inversion Recovery

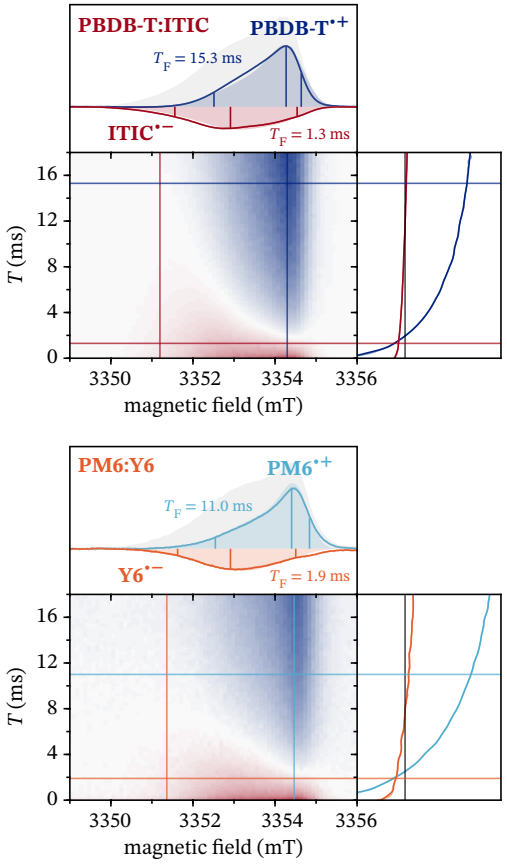

Fig. S3 W-band inversion recovery experiments on PBDB-T:ITIC and PM6:Y6 recorded as a function the inversion delay T and of the magnetic field at 20 K (red = negative echo signal, blue = positive echo signal). The right panel shows the inversion recovery traces extracted at two magnetic field positions (indicated by the lines in the 2D spectrum), while the top panel shows the EPR spectra extracted for different inversion delays T (indicated by lines in the 2D spectrum and the right panels) as well as the corresponding simulations with the parameters reported in Table 1. The full EPR spectrum recorded for a long T value (>200 ms), after complete recovery of the full echo signal, is also shown as grey shaded area.

S7 Comparison of Davies ENDOR results for different donor:acceptor blends

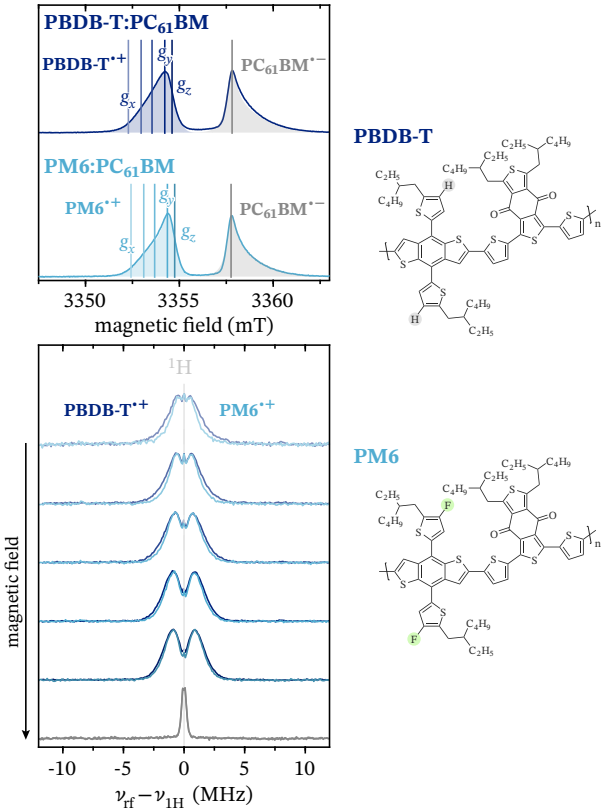

Fig. S4 Comparison of W-band ^{1}H Davies spectra for the two fullerene-acceptor-based blends, PBDB-T:$PC_{61}BM$ and PM6:$PC_{61}BM$, recorded at different magnetic field positions. The corresponding field positions with respect to the EPR spectra are indicated in the top panel. The difference between the two donor polymers, replacement of two protons on the thiophene sidechains with two fluorine nuclei, is highlighted in the molecular structures displayed on the right.

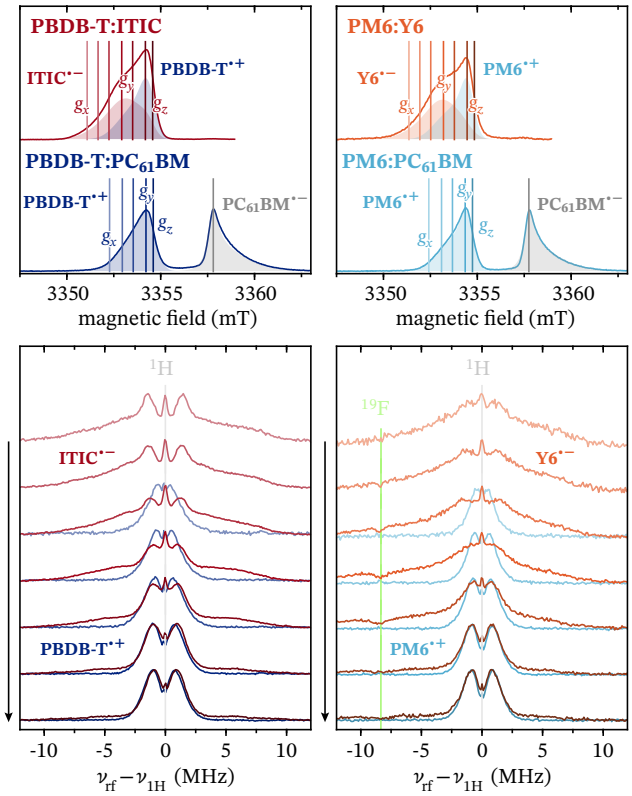

Fig. S5 Comparison of W-band ^{1}H Davies spectra recorded at different magnetic field positions for the two pairs of fullerene- and non-fullerene-acceptor-based blends sharing the same donor polymer: PBDB-T:$PC_{61}BM$ and PBDB-T:ITIC (*left*) and PM6:$PC_{61}BM$ and PM6:Y6 (*right*). The corresponding field positions with respect to the EPR spectra are indicated in the top panels.

S8 Comparison of Davies and Mims ENDOR spectra

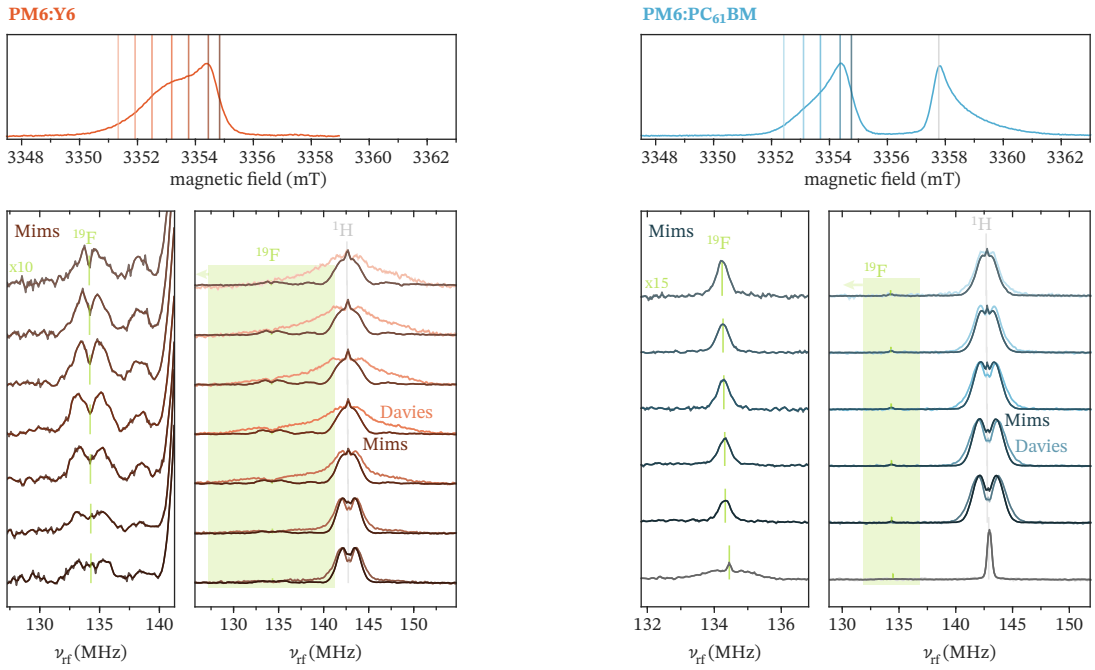

Fig. S6 Comparison of W-band ^{1}H Davies and Mims ENDOR spectra for the PM6:PC_{61}BM blend (*left*) and PM6:Y6 blend (*right*) recorded at different magnetic field positions at a temperature of 20 K (see the experimental methods section for additional experimental details). The bottom right panels show a comparison of the full ENDOR spectra recorded at each field position with the two different ENDOR techniques and the bottom left panels focus on the contributions from ^{19}F nuclei (region highlighted in green in the right panels). The top panels show the field positions with respect to the experimental W-band EPR spectra.

DFT modelling

S9 Spin densities and g-frames

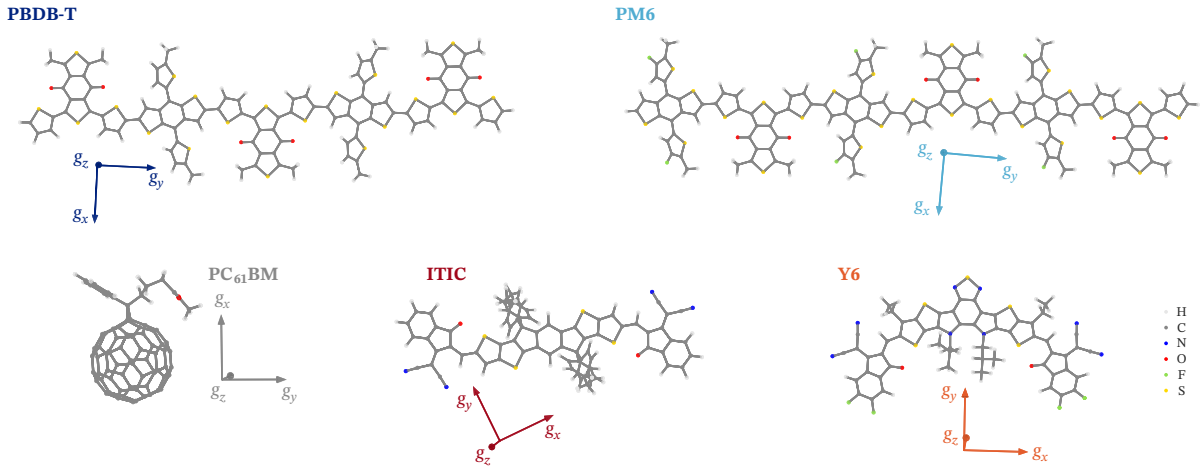

Fig. S7 Orientation of the principal g-axes with respect to the molecular structure for PBDB-T$^{\bullet+}$, PM6$^{\bullet+}$, $PC_{61}BM^{\bullet-}$, ITIC$^{\bullet-}$ and Y6$^{\bullet-}$. See discussion in the main text for details.

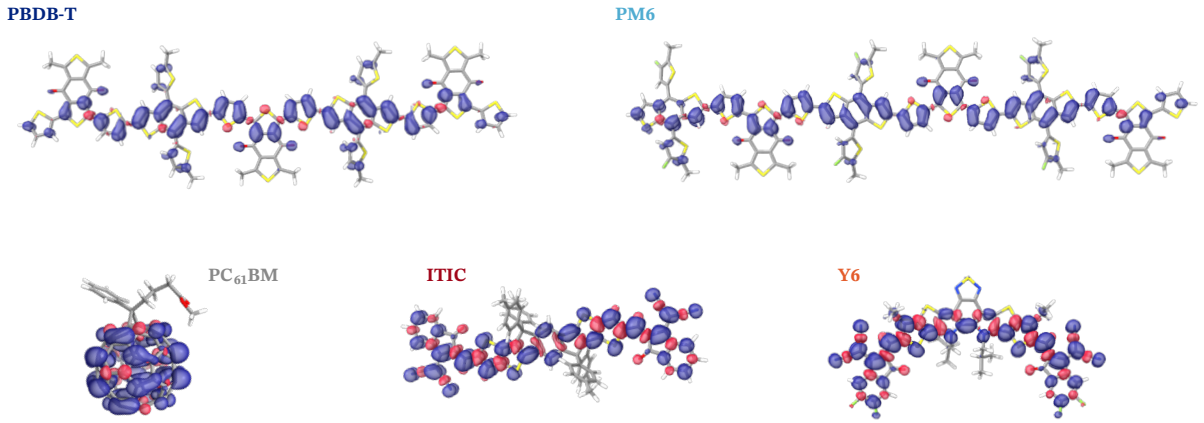

Fig. S8 Spin densities predicted by DFT (PBE0/EPRII) for PBDB-T$^{\bullet+}$, PM6$^{\bullet+}$, $PC_{61}BM^{\bullet-}$, ITIC$^{\bullet-}$ and Y6$^{\bullet-}$ (contour level $4\cdot10^{-4}$).

S10 Comparison of DFT models for donor and acceptor molecules

S10.1 Donor polymers

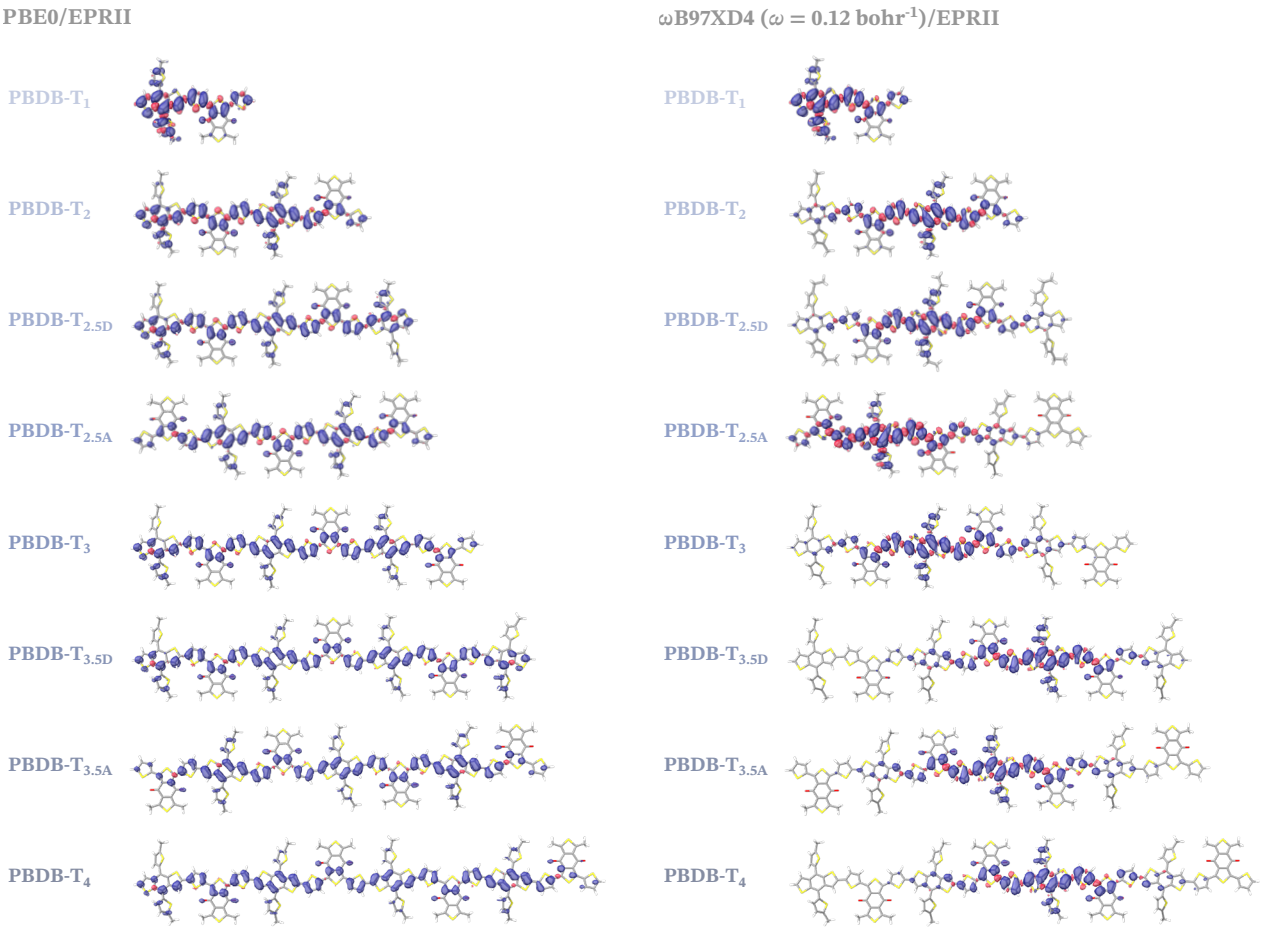

Fig. S9 Spin density distributions predicted by DFT for radical cations on PBDB-T chains of increasing lengths with the PBE0 hybrid functional (left) and with the range-separated hybrid ωB97XD4 functional with tuned range separation parameter (right). All spin densities are shown for the same contour level ($4 \cdot 10^{-4}$). For additional details see section S3.

.

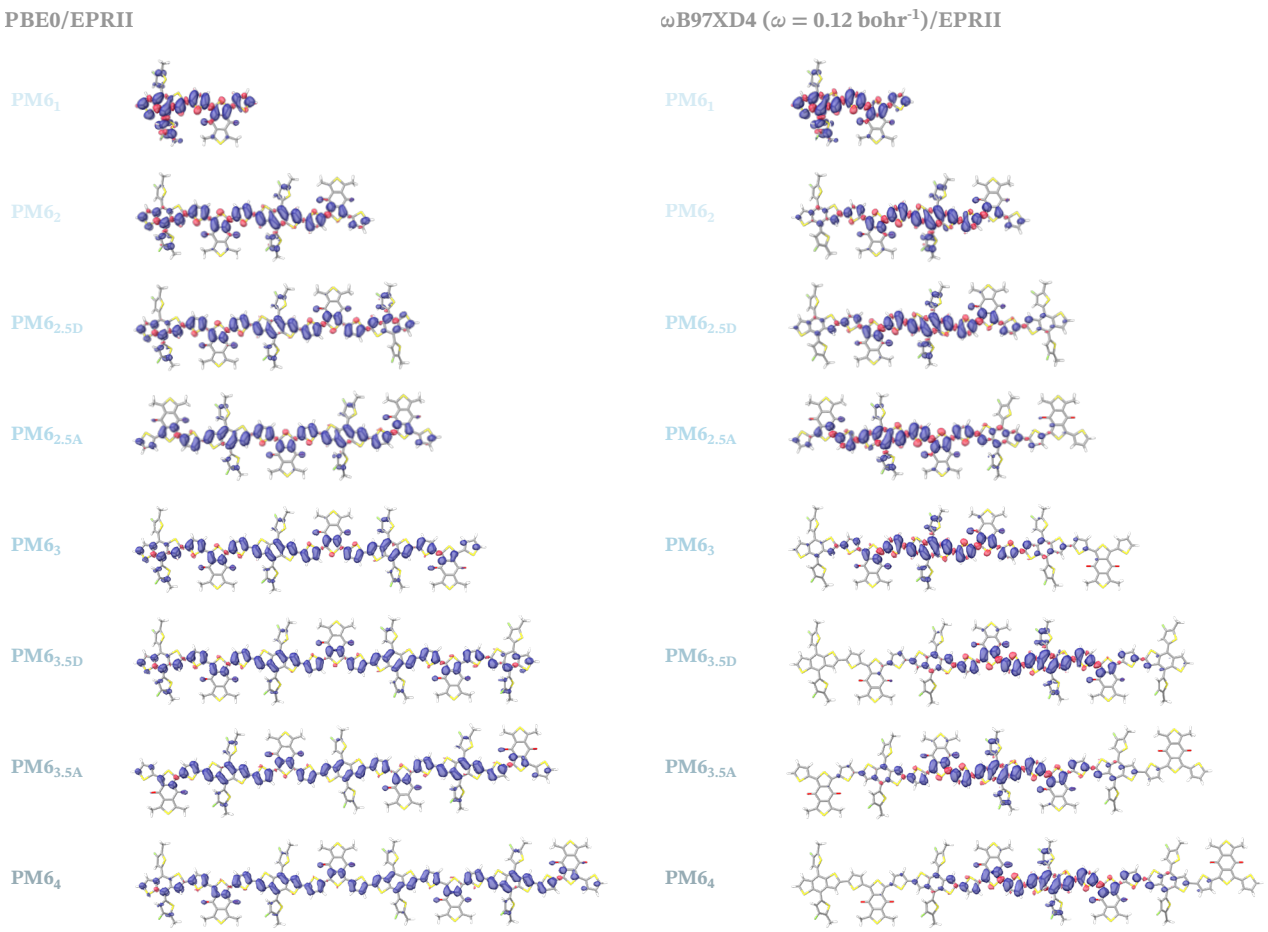

Fig. S10 Spin density distributions predicted by DFT for radical cations on PM6 chains of increasing lengths with the PBE0 hybrid functional (left) and with the range-separated hybrid ωB97XD4 functional with tuned range separation parameter (right). All spin densities are shown for the same contour level ($4 \cdot 10^{-4}$). For additional details see section S3.

S10.2 Acceptor molecules

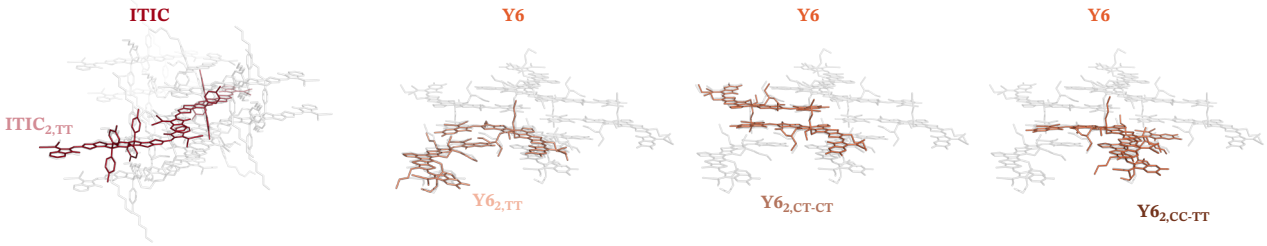

Fig. S11 Comparison of crystal structures for ITIC[15] and Y6[17] with the different geometry-optimised dimers $ITIC_{2,TT}$, $Y6_{2,TT}$, $Y6_{2,CT\text{-}CT}$, and $Y6_{2,CC\text{-}TT}$. The geometries were optimised at the BP86/def2-SVP level in ORCA.

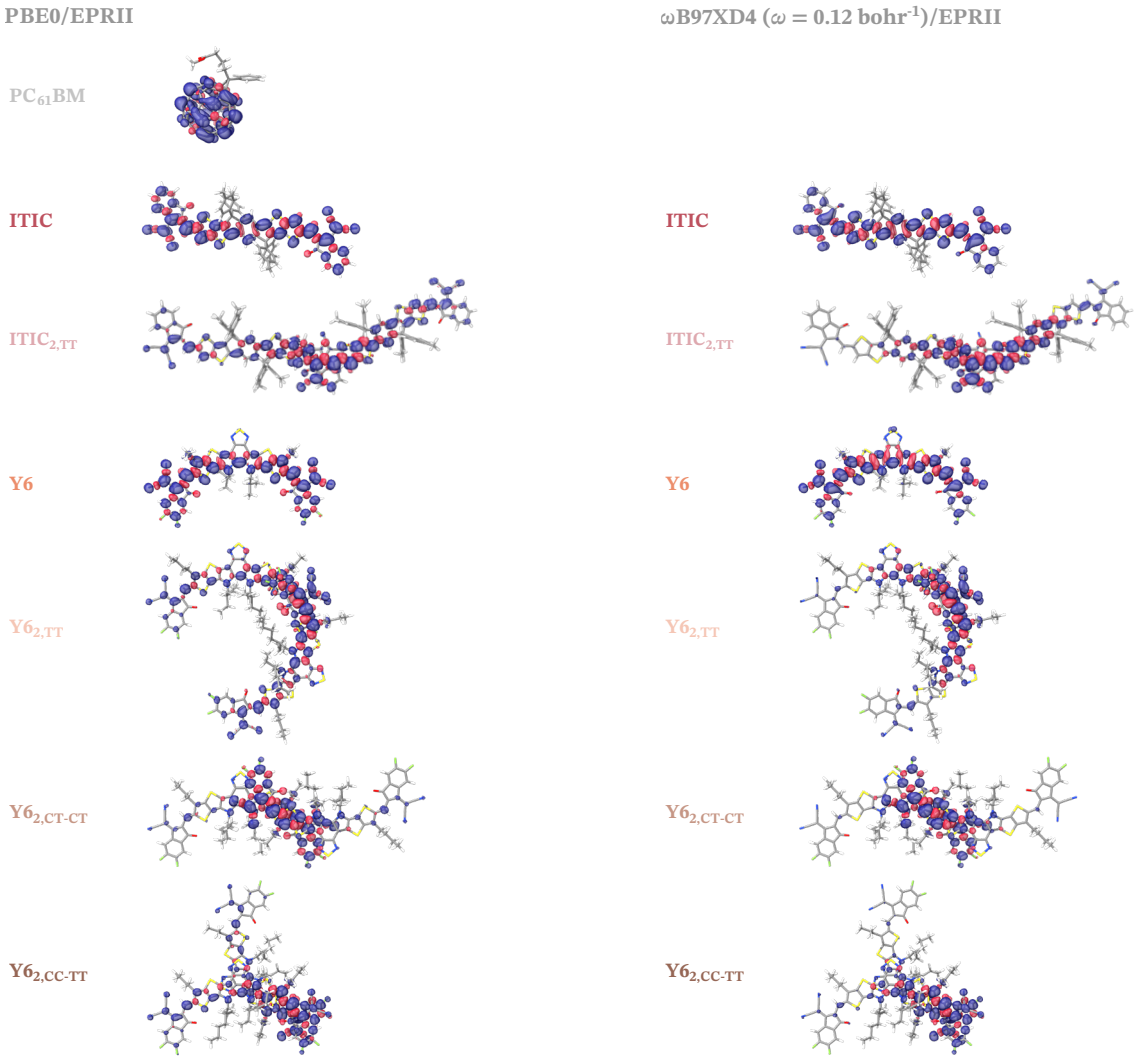

Fig. S12 Spin density distributions predicted by DFT for radical anions on $PC_{61}BM$, ITIC and a single molecule of Y6 as well as three dimers extracted from the crystal structure[17]. Results for calculations with the PBE0 hybrid functional are shown on the left and compared to results obtained with the range-separated hybrid ωB97XD4 functional with tuned range separation parameter on the right. All spin densities are shown for the same contour level ($4 \cdot 10^{-4}$). For additional details see section S3.

Additional ENDOR and HYSCORE simulations

S11 ENDOR simulations based on DFT results

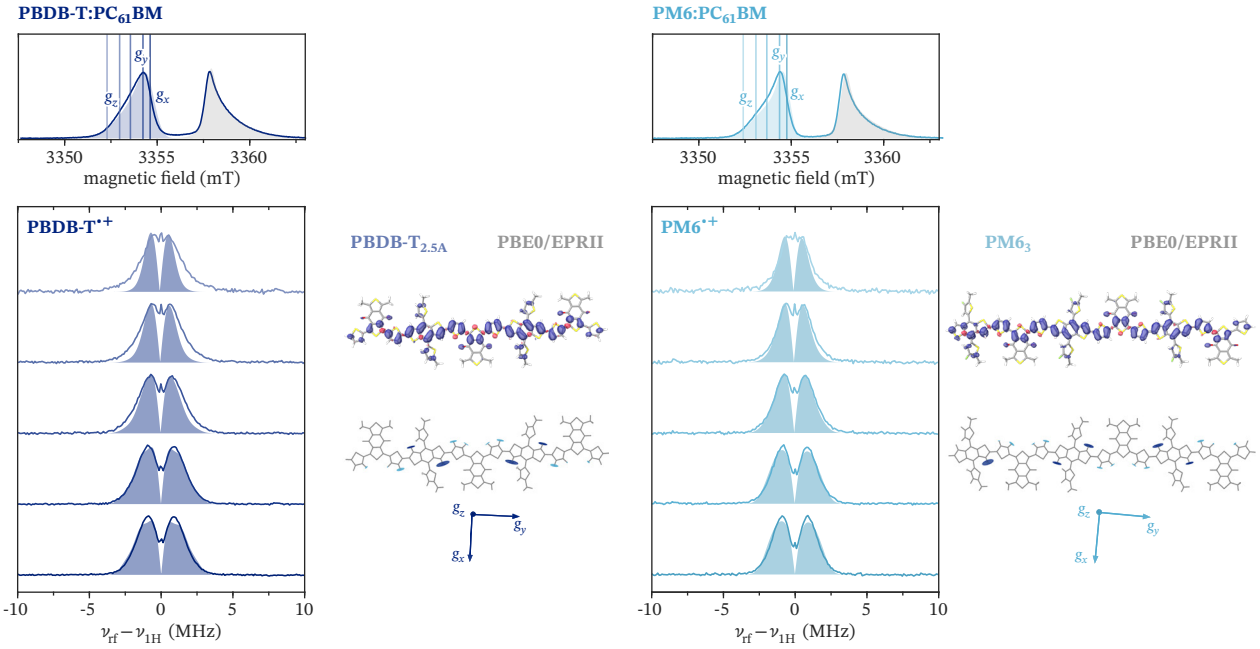

Fig. S13 Comparison of the experimental W-band ^{1}H ENDOR spectra recorded for PBDB-T$^{\bullet+}$ (*left*) and PM6$^{\bullet+}$ (*right*) at different field positions across the EPR spectrum with simulations based on hyperfine couplings predicted by DFT for the models giving the best agreement with the experimental data (PBDB-T$_{2.5A}$ and PM6$_3$ at the PBE0/EPRII level). The corresponding spin density distributions and the orientations of the hyperfine spheroids with respect to the molecular structure and g-frame are also shown.

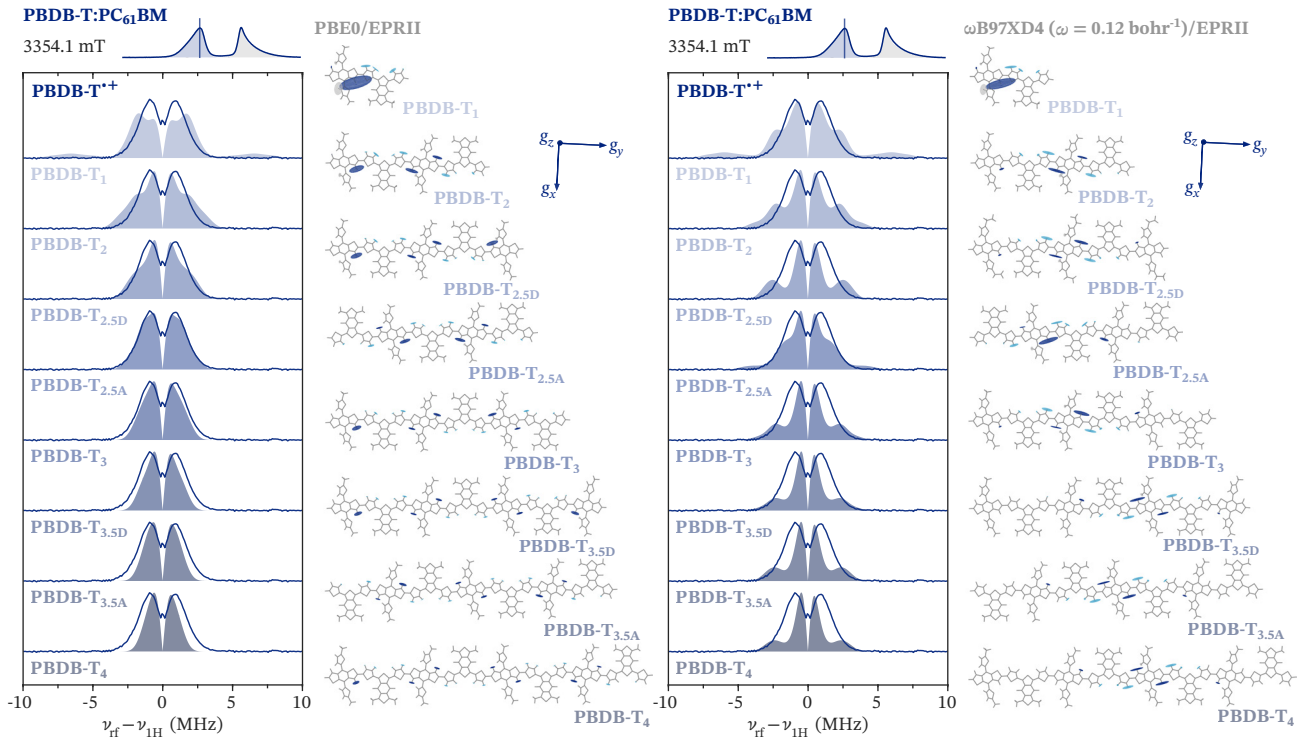

Fig. S14 Comparison of the experimental W-band ^{1}H ENDOR spectrum recorded for PBDB-T$^{\bullet+}$ at the field position corresponding to the maximum (g_y, g_z) with simulations based on hyperfine couplings predicted by DFT for models of increasing chain length with one to four repeat units at the PBE0/EPRII (*left*) and at the ωB97X-D4/EPRII (*right*) level (with non-empirically optimised ω, see section S3 for details). The orientations of the hyperfine spheroids with respect to the molecular structure and g-frame are also shown (for the corresponding spin density distributions see Fig. S9).

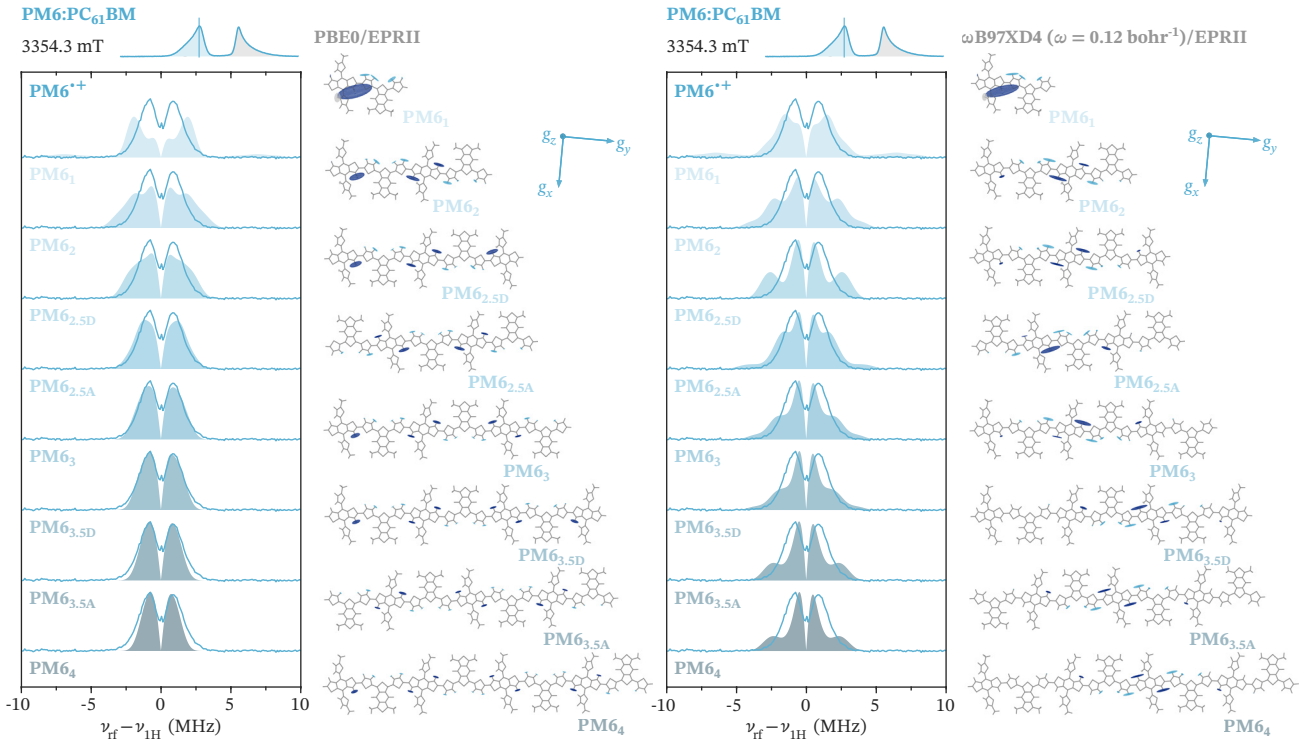

Fig. S15 Comparison of the experimental W-band ^{1}H ENDOR spectrum recorded for PM6$^{\bullet+}$ at the field position corresponding to the maximum (g_y, g_z) with simulations based on hyperfine couplings predicted by DFT for models of increasing chain length with one to four repeat units at the PBE0/EPRII (*left*) and at the ωB97X-D4/EPRII (*right*) level (with non-empirically optimised ω, see section S3 for details). The orientations of the hyperfine spheroids with respect to the molecular structure and *g*-frame are also shown (for the corresponding spin density distributions see Fig. S10).

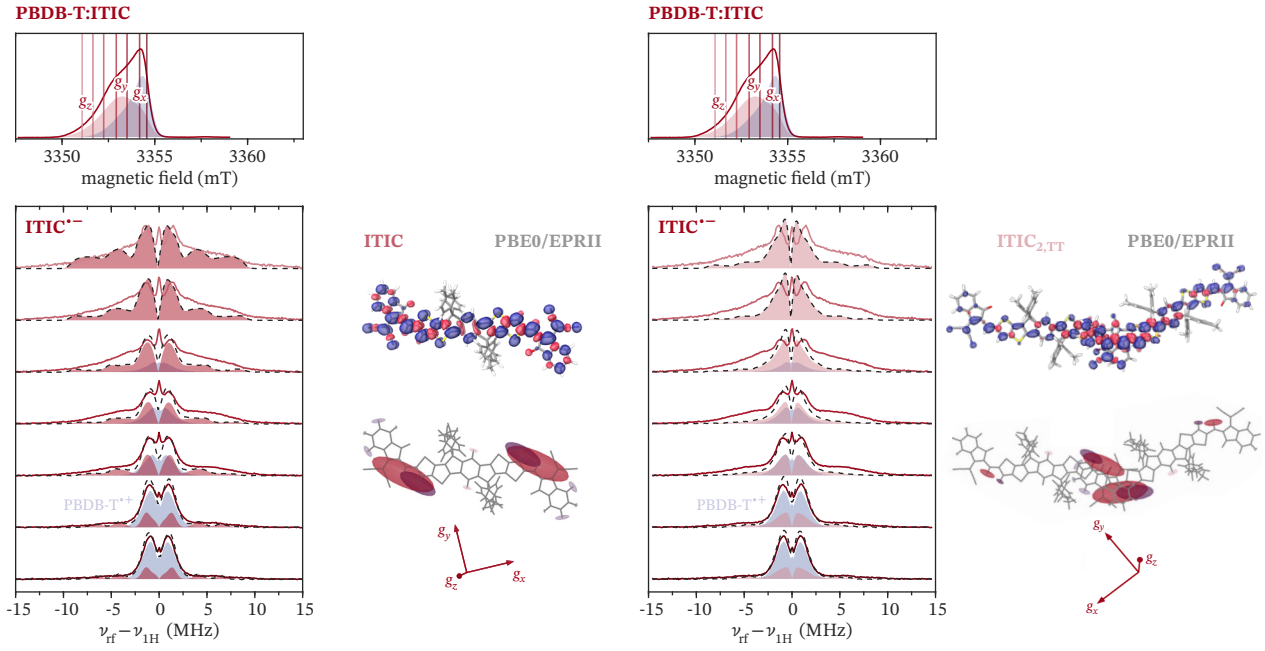

Fig. S16 Comparison of the experimental W-band ^{1}H ENDOR spectra recorded for ITIC$^{\bullet-}$ at different field positions across the EPR spectrum with simulations based on hyperfine couplings predicted by DFT for a single ITIC molecule (*left*) and for a pair of ITIC molecules with overlapping terminal groups (*right*) at the PBE0/EPRII level. The corresponding spin density distributions and the orientations of the hyperfine spheroids with respect to the molecular structure and *g*-frame are also shown.

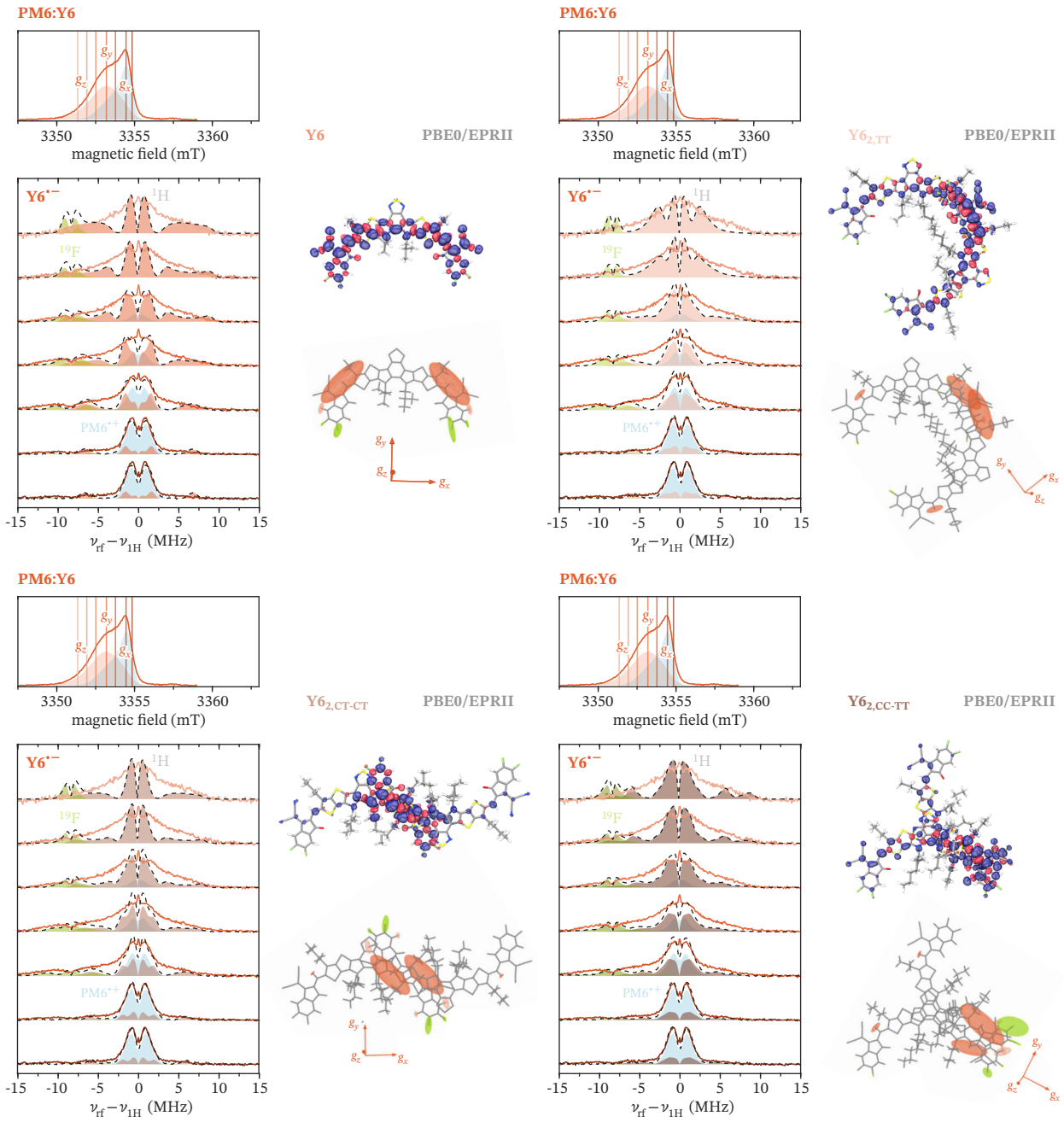

Fig. S17 Comparison of the experimental W-band ^{1}H ENDOR spectra recorded for Y6$^{\bullet-}$ at different field positions across the EPR spectrum with simulations based on hyperfine couplings predicted by DFT for a single Y6 molecule and three different dimers with different pair configurations, Y6$_{2,TT}$, Y6$_{2,CT-CT}$ and Y6$_{2,CC-TT}$ (at the PBE0/EPRII level). The corresponding spin density distributions and the orientations of the hyperfine spheroids with respect to the molecular structure and g-frame are also shown.

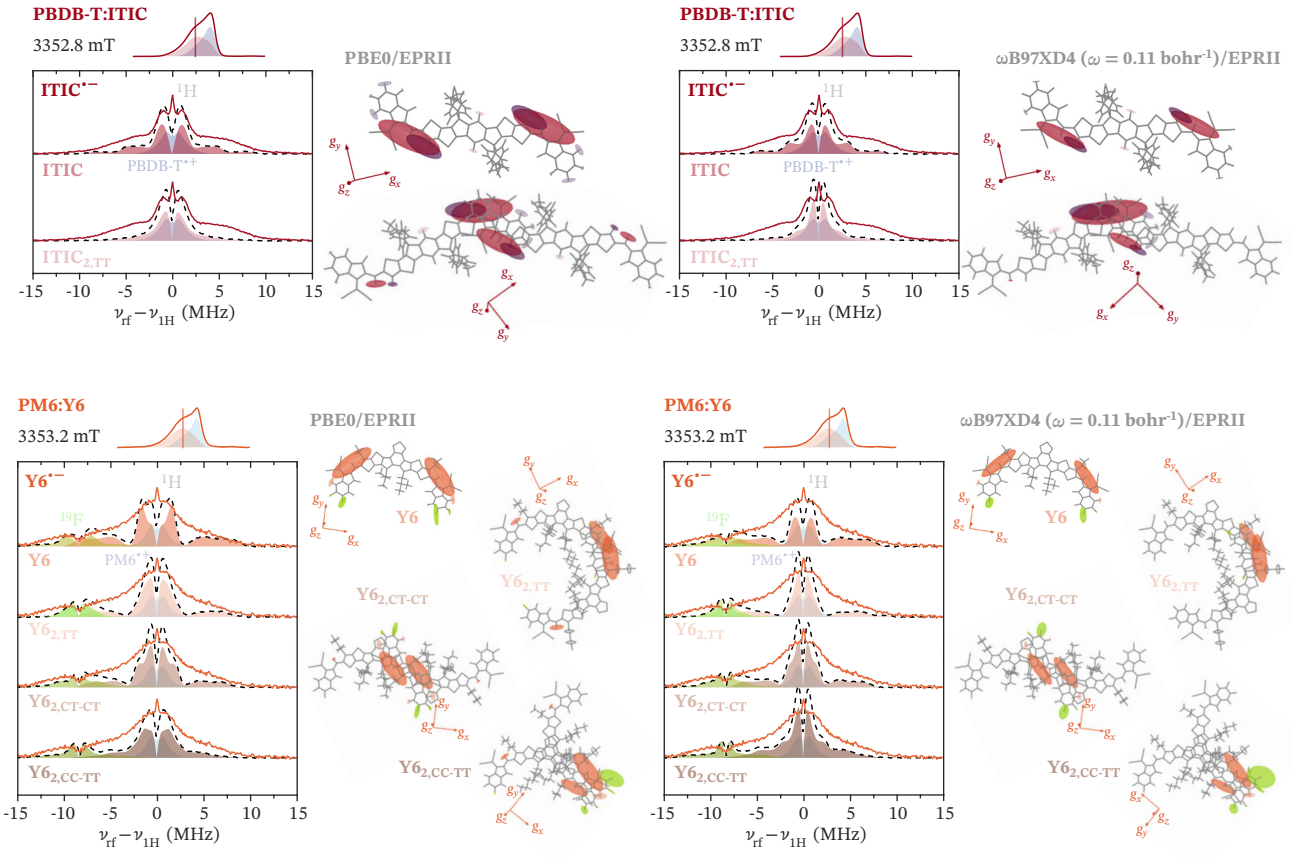

Fig. S18 Comparison of the experimental W-band ^{1}H ENDOR spectrum recorded for ITIC$^{\bullet-}$ and PM6$^{\bullet+}$ at the field positions corresponding to the maximum (g_y) with simulations based on hyperfine couplings predicted by DFT for different molecular models, including a single molecule and different dimer configurations, at the PBE0/EPRII (*left*) and at the ωB97X-D4/EPRII (*right*) level (with non-empirically optimised ω, see section S3 for details). The orientations of the hyperfine spheroids with respect to the molecular structure and g-frame are also shown (for the corresponding spin density distributions see Fig. S12).

S12 ENDOR simulations based on regularised-least-squares fitting

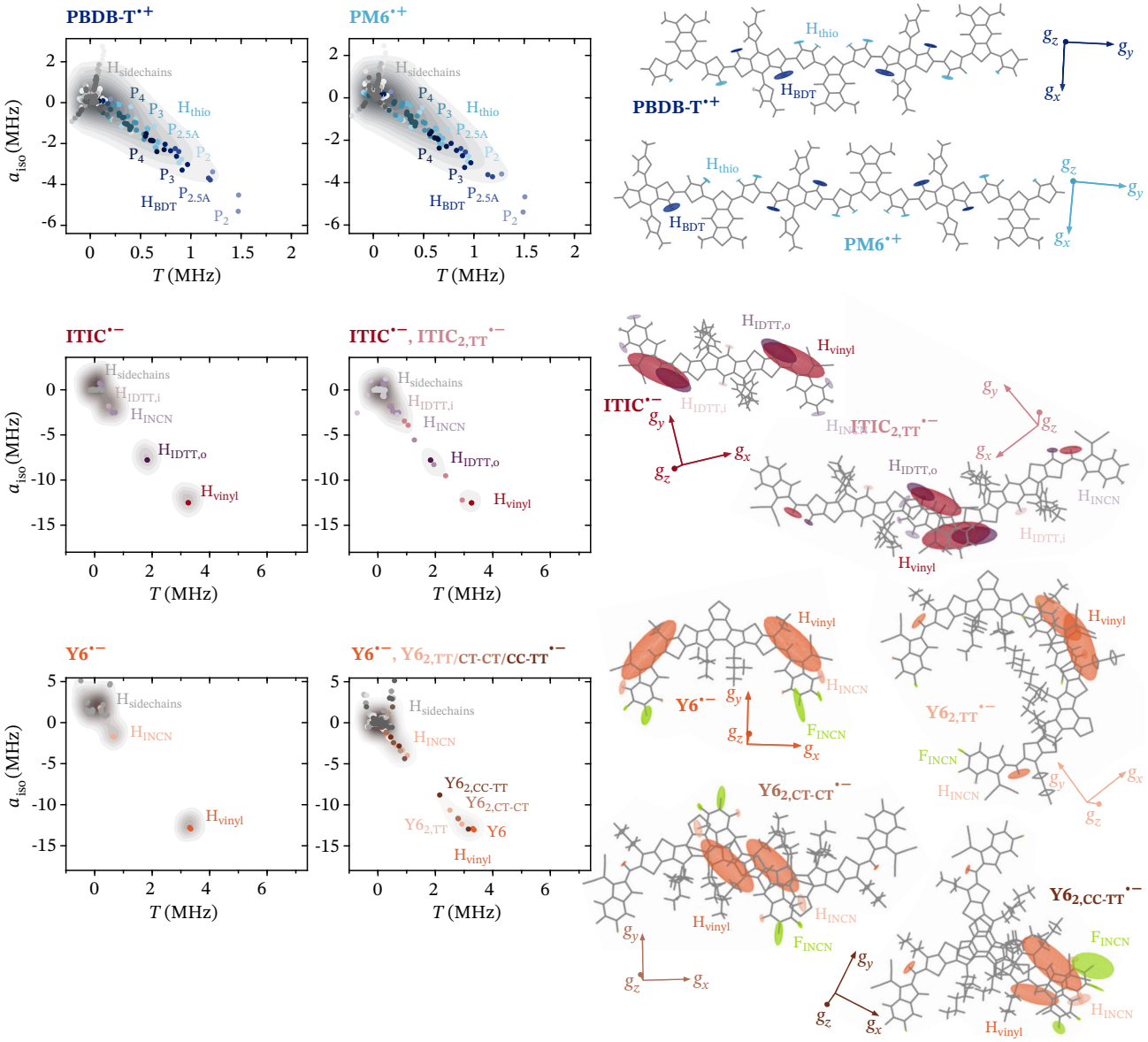

Fig. S19 Prior probability distributions $P(a_{iso}, T, \eta, \alpha_{ID})$ for PBDB-T$^{\bullet+}$, PM6$^{\bullet+}$, ITIC$^{\bullet-}$ and Y6$^{\bullet-}$ derived from the results of DFT calculations and projected onto the the a_{iso}, T space. Individual contributions of different types of protons determined with PBE0/EPRII calculations on the constructed molecular models are displayed as dots and colour-coded based on type of proton and molecular model. The DFT-predicted hyperfine spheroids are displayed with respect to the molecular structure for selected models.

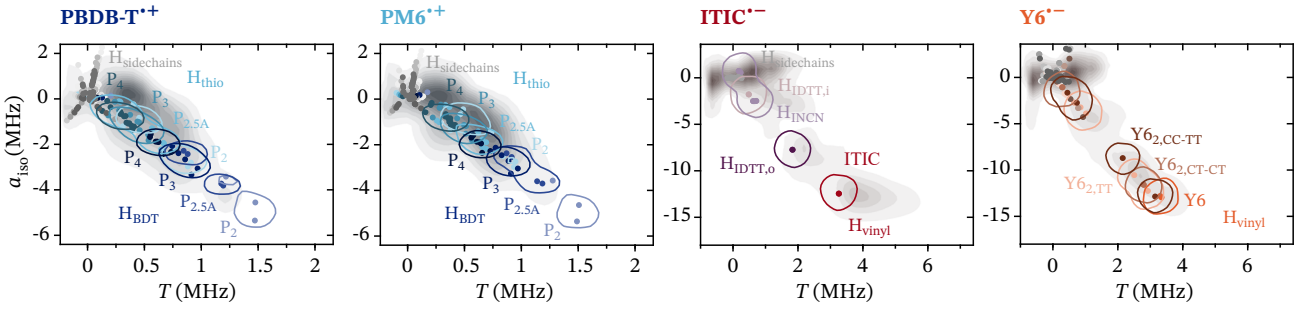

Fig. S20 Projection of the probability distributions $P(a_{iso}, T, \eta, \alpha_{ID})$ for PBDB-T$^{\bullet+}$, PM6$^{\bullet+}$, ITIC$^{\bullet-}$ and Y6$^{\bullet-}$ obtained from regularised least-squares fitting of the experimental ENDOR data onto the the a_{iso}, T space. Individual contributions of different types of protons determined with PBE0/EPRII calculations on different molecular models are displayed as dots and colour-coded based on type of proton and molecular model.

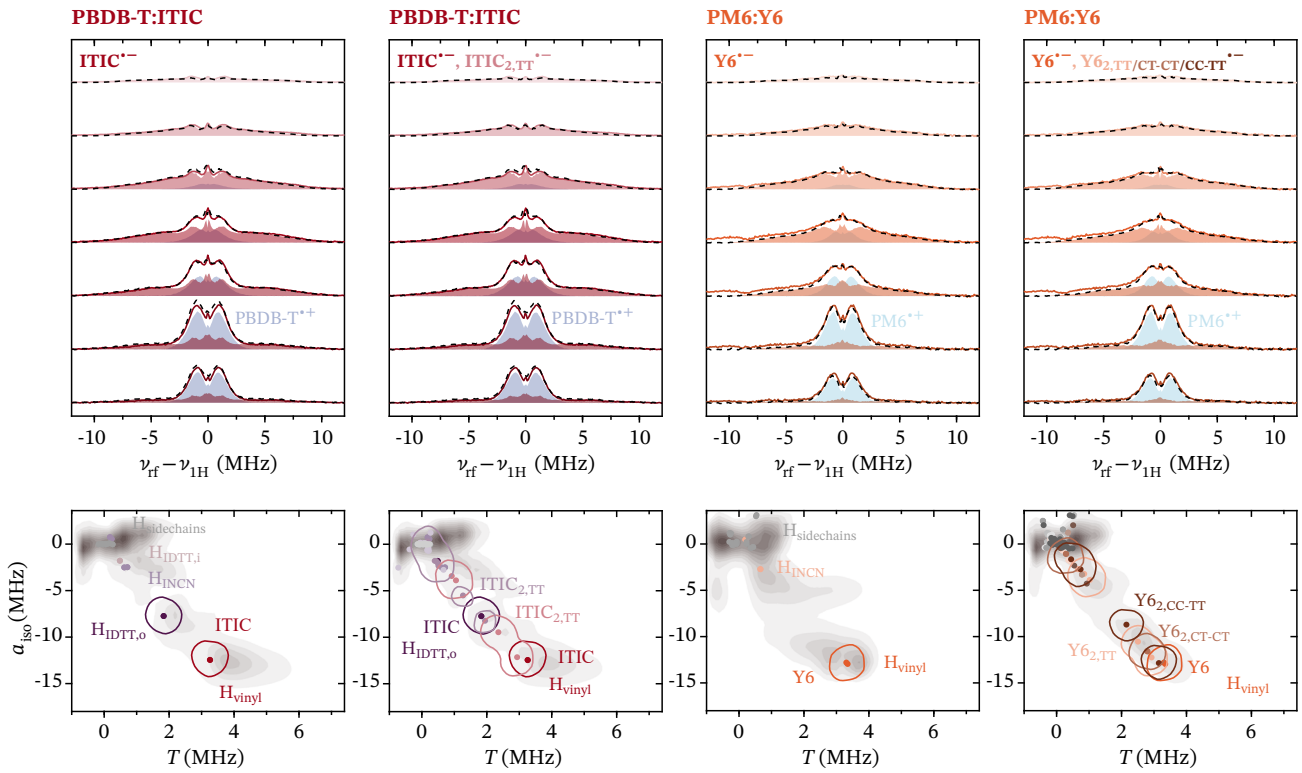

Fig. S21 Comparison of the experimental W-band ENDOR spectra recorded for the PBDB-T:ITIC and PM6:Y6 blends with the results of regularised least-squares fitting with a penalty term based on the agreement of the probability distribution $P(a_{iso}, T, \eta, \alpha_{ID})$ with a prior probability distribution constructed based on DFT calculations on the single ITIC or Y6 molecule or additionally including pairs of molecules modelled based on the crystal structures (see section S3 and Fig. S11 for details). A projection of the final probability distribution onto the a_{iso}, T space is shown in the bottom panels (see the main text and section S4.3 in the SI for details).

S13 HYSCORE simulations based on DFT results

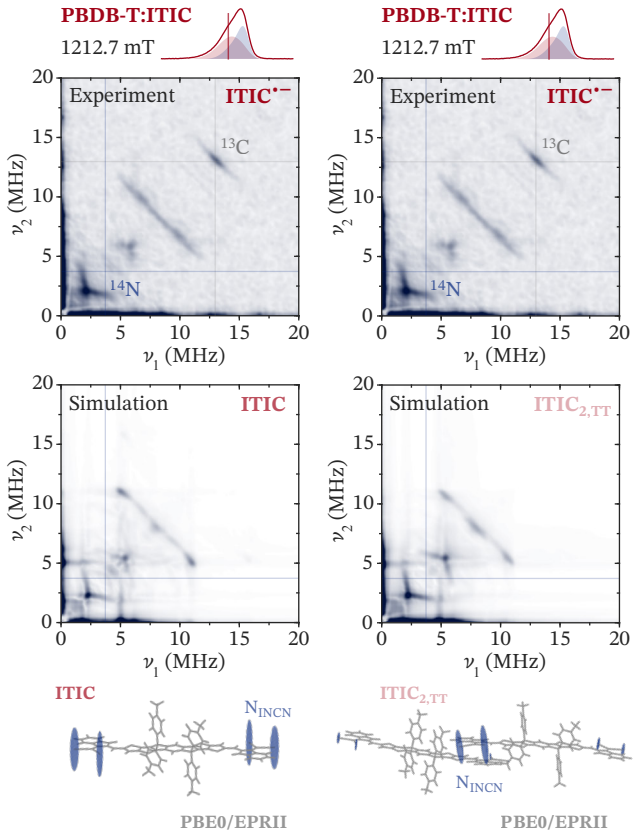

Fig. S22 Experimental Q-band ^{14}N HYSCORE spectra (*top*) for the PBDB-T:ITIC blend at the field position corresponding to the maximum of the ITIC$^{\bullet-}$ spectrum and corresponding simulations (*bottom*) based on ^{14}N hyperfine couplings predicted by DFT calculations for a negative charge on an isolated ITIC molecule and an ITIC dimer extracted from the crystal structure[15]. The molecular structures and calculated ^{14}N hyperfine spheroids are shown at the bottom of the figure. Additional experimental details can be found in section S2.5 in the SI.

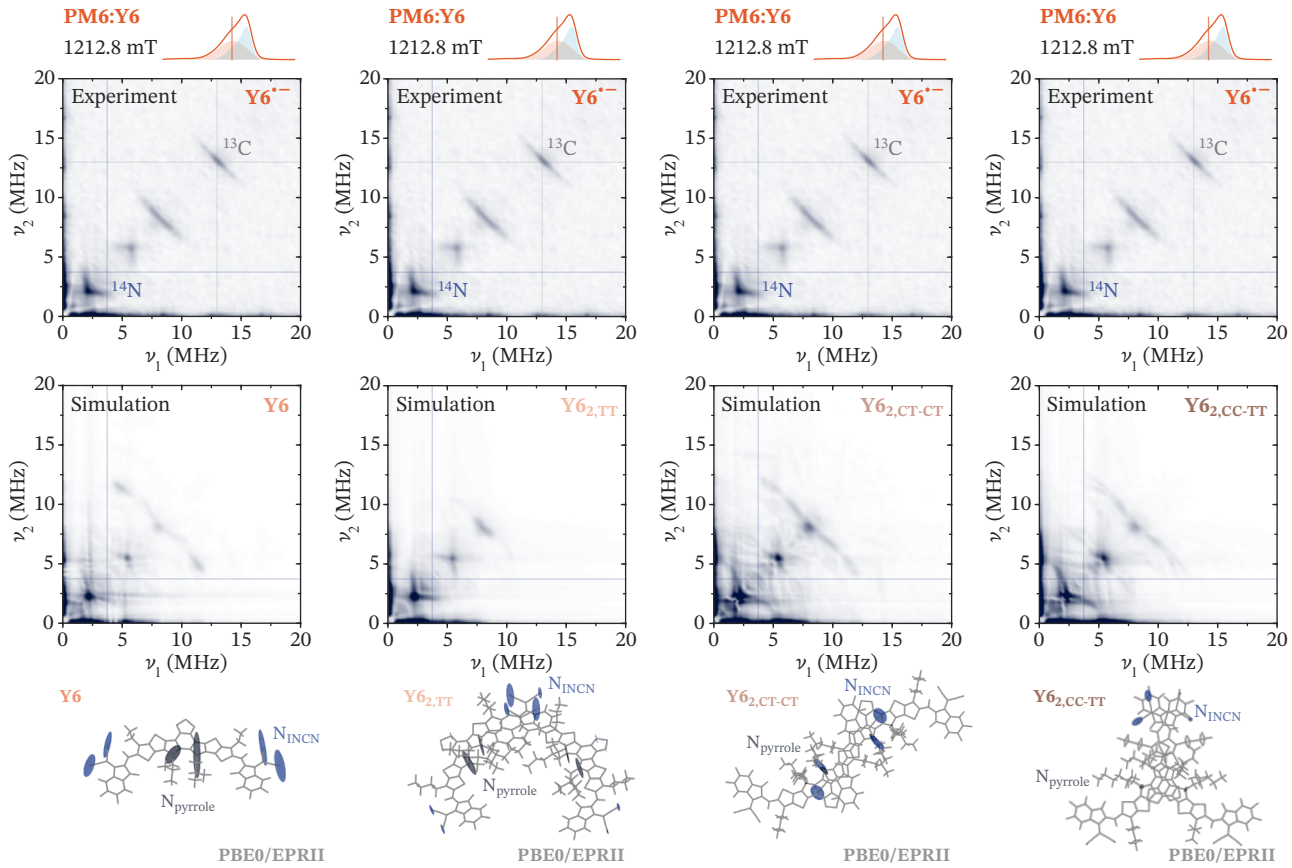

Fig. S23 Experimental Q-band ^{14}N HYSCORE spectra (*top*) for the PM6:Y6 blend at the field position corresponding to the maximum of the Y6$^{\bullet-}$ spectrum and corresponding simulations (*bottom*) based on ^{14}N hyperfine couplings predicted by DFT calculations for a negative charge on an isolated Y6 molecule and three types of Y6 dimers extracted from the crystal structure[17]. The molecular structures and calculated ^{14}N hyperfine spheroids are shown at the bottom of the figure. Additional experimental details can be found in section S2.5 in the SI.

References

1 J. A. Bartelt, Z. M. Beiley, E. T. Hoke, W. R. Mateker, J. D. Douglas, B. A. Collins, J. R. Tumbleston, K. R. Graham, A. Amassian, H. Ade, J. M. J. Fréchet, M. F. Toney and M. D. McGehee, *Adv. Energy Mater.*, 2013, **3**, 364–374.

2 N. Y. Doumon, G. Wang, R. C. Chiechi and L. J. A. Koster, *J. Mater. Chem. C*, 2017, **5**, 6611–6619.

3 W. Zhao, D. Qian, S. Zhang, S. Li, O. Inganäs, F. Gao and J. Hou, *Adv. Mater.*, 2016, **28**, 4734–4739.

4 M. Zhang, X. Guo, W. Ma, H. Ade and J. Hou, *Adv. Mater.*, 2015, **27**, 4655–4660.

5 J. Yuan, Y. Zhang, J. Yuan, Y. Zhang, L. Zhou, G. Zhang, H.-L. Yip, T.-K. Lau, X. Lu, C. Zhu, H. Peng, P. A. Johnson, M. Leclerc, Y. Cao, J. Ulanski, Y. Li and Y. Zou, *Joule*, 2019, **3**, 1140–1151.

6 E. J. Reijerse, F. Lendzian, R. A. Isaacson and W. Lubitz, *J. Magn. Reson.*, 2012, **214**, 237–243.

7 J. J. Wittmann, T. V. Can, M. Eckardt, W. Harneit, R. G. Griffin and B. Corzilius, *J. Magn. Reson.*, 2018, **290**, 12–17.

8 B. Kasumaj and S. Stoll, *J. Magn. Reson.*, 2008, **190**, 233–247.

9 F. Neese, *WIRES: Comput. Mol. Sci.*, 2012, **2**, 73–78.

10 F. Neese, *WIRES: Comput. Mol. Sci.*, 2022, **12**, e1606–1–15.

11 F. Neese, *J. Comput. Chem.*, 2003, **24**, 1740–1747.

12 F. Neese, F. Wennmohs, A. Hansen and U. Becker, *Chem. Phys.*, 2009, **356**, 98–109.

13 B. Helmich-Paris, B. de Souza, F. Neese and R. Izsák, *J. Chem. Phys.*, 2021, **155**, 104109–1–14.

14 F. Neese, *J. Comput. Chem.*, 2023, **44**, 381–396.

15 T. J. Aldrich, M. Matta, W. Zhu, S. M. Swick, C. L. Stern, G. C. Schatz, A. Facchetti, F. S. Melkonyan and T. J. Marks, *J. Am. Chem. Soc.*, 2019, **141**, 3274–3287.

16 C. Xiao, C. Li, F. Liu, L. Zhang and W. Li, *J. Mater. Chem. C*, 2020, **6**, 5370–5374.

17 G. Zhang, X. K. Chen, J. Xiao, P. C. Y. Chow, M. Ren, G. Kupgan, X. Jiao, C. C. S. Chan, X. Du, R. Xia, Z. Chen, J. Yuan, Y. Zhang, S. Zhang, Y. Liu, Y. Zou, H. Yan, K. S. Wong, V. Coropceanu, N. Li, C. J. Brabec, J.-L. Brédas, H. L. Yip and Y. Cao, *Nat. Commun.*, 2020, **11**, 3943–1–10.

18 N. Mardirossian and M. Head-Gordon, *Phys. Chem. Chem. Phys.*, 2014, **16**, 9904–9924.

19 A. Najibi and L. Goerigk, *J. Comput. Chem.*, 2020, **41**, 2562–2572.

20 F. Weigend and R. Ahlrichs, *Phys. Chem. Chem. Phys.*, 2005, **7**, 3297–3305.

21 F. Weigend, *Phys. Chem. Chem. Phys.*, 2006, **8**, 1057–1065.

22 S. Grimme, J. Antony, S. Ehrlich and H. Krieg, *J. Chem. Phys.*, 2010, **132**, 154104–1–19.

23 S. Grimme, S. Ehrlich and L. Goerigk, *J. Comput. Chem.*, 2011, **32**, 1456–1465.

24 E. Caldeweyher, C. Bannwarth and S. Grimme, *J. Chem. Phys.*, 2017, **147**, 034112–1–7.

25 E. Caldeweyher, S. Ehlert, A. Hansen, H. Neugebauer, S. Spicher, C. Bannwarth and S. Grimme, *J. Chem. Phys.*, 2019, **150**, 154122–1–19.

26 E. Caldeweyher, J. M. Mewes, S. Ehlert and S. Grimme, *Phys. Chem. Chem. Phys.*, 2020, **22**, 8499–8512.

27 R. Baer, E. Livshits and U. Salzner, *Annu. Rev. Phys. Chem.*, 2010, **61**, 85–109.

28 T. Stein, L. Kronik and R. Baer, *J. Am. Chem. Soc.*, 2009, **131**, 2818–2820.

29 L. N. Anderson, M. B. Oviedo and B. M. Wong, *J. Chem. Theory Comput.*, 2017, **13**, 1656–1666.

30 T. Körzdörfer, J. S. Sears, C. Sutton and J.-L. Brédas, *J. Chem. Phys.*, 2011, **135**, 204107–1–6.

31 K. J. Thorley, *J. Phys. Chem. B*, 2023, **127**, 5102–5114.

32 M. C. Scharber and N. S. Sariciftci, *Progress in Polymer Science*, 2013, **38**, 1929–1940.

33 S. Gélinas, A. Rao, A. Kumar, S. L. Smith, A. W. Chin, J. Clark, T. S. van der Poll, G. C. Bazan and R. H. Friend, *Science*, 2014, **343**, 512–517.

34 M. Van Landeghem, W. Maes, E. Goovaerts and S. Van Doorslaer, *J. Magn. Reson.*, 2018, **288**, 1–10.

35 F. Neese, *J. Chem. Phys.*, 2001, **115**, 11080–11096.

36 F. Neese, *J. Phys. Chem. A*, 2001, **105**, 4290–4299.

37 F. Neese, *J. Chem. Phys.*, 2005, **122**, 034107–1–13.

38 F. Neese, *eMagRes*, 2017, **6**, 1–22.

39 V. Barone, *Recent Advances in Density Functional Methods*, World Scientific Publ. Co., Singapore, 1995, vol. 1, ch. 8, pp. 287–334.

40 N. Rega, M. Cossi and V. Barone, *J. Chem. Phys.*, 1996, **105**, 11060–11067.

41 S. Huzinaga, *J. Chem. Phys.*, 1965, **42**, 1293–1302.

42 W. Kutzelnigg, U. Fleischer and M. Schindler, *NMR Basic Principles and Progress Vol. 23*, Springer, Heidelberg, 1990, p. 165.

43 S. Stoll and A. Schweiger, *J. Magn. Reson.*, 2006, **178**, 42–55.

44 S. Stoll and R. D. Britt, *Phys. Chem. Chem. Phys.*, 2009, **11**, 6614–6625.

45 S. Pribitzer, D. Mannikko and S. Stoll, *Phys. Chem. Chem. Phys.*, 2021, **23**, 8326–8335.

46 N. M. Atherton, *Principles of Electron Spin Resonance*, PTR Prentice Hall, New York, 1993.

47 A. Schweiger and G. Jeschke, *Principles of pulse electron paramagnetic resonance*, Oxford University Press, 2001.

48 R. Bro and S. De Jong, *J. Chemometrics*, 1997, **11**, 393–401.

49 A. V. Astashkin and A. Kawamori, *J. Magn. Reson.*, 1998, **135**, 406–417.

50 T. Maly and T. F. Prisner, *J. Magn. Reson.*, 2004, **170**, 88–96.

51 T. Maly, F. MacMillan, K. Zwicker, N. Kashani-Poor,

U. Brandt and T. F. Prisner, *Biochemistry*, 2004, **43**, 3969–3978.